Design of a New Cable-Driven Manipulator with a Large Open Lumen: Preliminary Applications in the Minimally-Invasive Removal of Osteolysis

Michael D.M. Kutzer, Sean M. Segreti, Christopher Y. Brown, Russell H. Taylor, Simon C. Mears, and Mehran Armand

***Abstract*— A dexterous manipulator (DM) with a large open lumen is presented. The manipulator is designed for surgical applications with a preliminary focus on the removal of osteolysis formed behind the acetabular shell of primary total hip arthroplasties (THAs). The manipulator is constructed from two nested superelastic nitinol tubes enabling lengthwise channels for drive cables. Notches in the nested assembly provide reliable bending under applied cable tension producing kinematics that can be effectively modeled as a series of rigid vertebrae connected using pin joints. The manipulator is controlled in plane with two independently actuated cables in a pull-pull configuration. For the purpose of the procedure, the manipulator is mounted on a Z-θ stage adding a translational and rotational degree of freedom (DOF) along the axis of the manipulator. Preliminary experimental results demonstrate the initial modeling and control of the manipulator.**

***Index Terms*— Snake-like robot, Dexterous manipulator, Flexible manipulator, Medical robot, Active cannula, Medical applications**

I. Introduction

Component wear and osteolysis (active resorption of bone around components) continues to be the primary phenomenon responsible for shortening the expected life span of total hip arthroplasty (THA) procedures. Among other things, wear of the polyethylene liner (generally found between the articulating femoral and acetabular components of the THA) leads to the formation of polyethylene particles that cause macrophage activation and osteolysis of the bone surrounding the implant. If left unmonitored and untreated, eventually fracture of bone surrounding the implant and/or component loosening with the potential of catastrophic failure (i.e. the implant becomes fully disconnected from the bone) will occur. Revision surgeries aim at eliminating the particle debris, removing all osteolytic lesions from the bone and other tissues, and replacing the worn polyethylene liner. A minimally-invasive approach attempts to preserve acetabular and femoral components of the THA, as long as they are firmly fixed to the bone, and only replace the polyethylene liner. This will help to avoid the risk of introducing fracture due to the removal of the acetabular component.

In minimally-invasive approaches, lesions are accessed either through existing screw holes of the well-fixed metal portion of the acetabular component or by drilling additional holes into the cortical bone of the pelvis. Here, the major challenges for the surgeon are the debridement of the lesion, determining that the lesion is fully debrided, grafting the debrided lesion, and determining that the lesion is fully bone grafted. Studies suggest that on average less than half of the lesion is grafted when this procedure is performed manually with existing instruments [1]. Revision procedures, therefore, will highly benefit from the use of instruments with high dexterity and potentially instruments that are robotically assisted to access these very difficult to reach areas within the pelvis (Fig. 1).

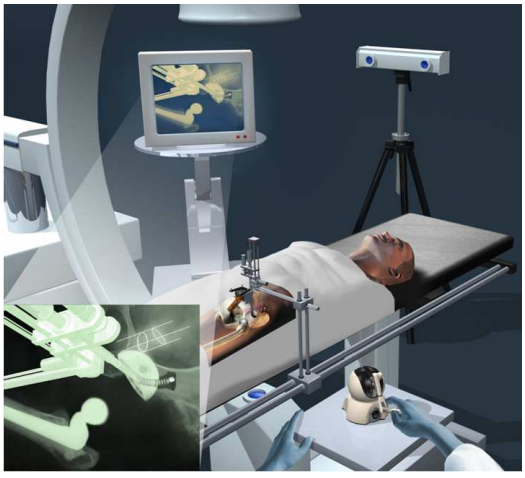

Fig. 1. Conceptual depiction of revision surgery highlighting the acetabular shell with removed polyethylene liner, and the dexterous manipulator accessing an osteolytic lesion through a screw hole.

In this paper we present the design, fabrication, preliminary control, and modeling of a new dexterous manipulator (DM): a snake-like cable-driven cannula that can be used to access osteolytic lesions formed behind the acetabular shell of a THA through the lumen of a larger, rigid guide cannula.

This work was supported by the Johns Hopkins University and Independent Research and Development funds provided by the Johns Hopkins University Applied Physics Laboratory.

M. Kutzer, C. Brown, and M. Armand are with the Milton S. Eisenhower Research Center, Johns Hopkins University Applied Physics Laboratory, Laurel, Maryland. {Michael.Kutzer, Christopher.Brown, Mehran.Armand}@jhuapl.edu

S. Segreti is with the A. James Clark School of Engineering at the University of Maryland, College Park and works as an intern at the Johns Hopkins University Applied Physics Laboratory, Laurel, Maryland. ssegreti@umd.edu

S. Mears is with the Department of Orthopaedic Surgery, Johns Hopkins Bayview Medical Center, Baltimore, Maryland. smears1@jhmi.edu

R. Taylor, M. Kutzer, and M. Armand are with the Laboratory for Computational Sensing and Robotics (LCSR), Johns Hopkins University, Baltimore, Maryland. {rht, mkutzer1, marmand2}@jhu.edu

The proposed goal of the procedure is to orient the lumen of the DM toward different parts of the lesion cavity and introduce various tools on flexible stems. A typical sequence may involve (1) accessing the lesion through existing screw holes or through holes drilled in the cortical bone of the pelvis; (2) inserting a rigid guide cannula to provide a reliable point of access; (3) inserting the DM through the rigid guide cannula; (4) inserting and actuating various combinations of metal brushes, pincers, water jets, and suction intermittently through the DM while the DM moves throughout the lesion; (5) introducing and actuating drilling tools through the DM to remove hardened tissue lining the lesion; (6) performing a final cleaning and inspection procedure by intermittently inserting combinations of water jets, suction, and a flexible endoscope; and (7) bone graft delivery or injecting poly(methyl methacrylate) (PMMA) bone cement through the lumen of the DM.

There is a body of work in the design and application of snake-like manipulators for minimally-invasive surgery (MIS) (e.g. [2]–[12]). The hyper-redundant dexterous manipulators used for MIS are usually designed for carrying diagnostic tools (e.g. endoscopic and arthroscopic surgery [2]), and/or performing tasks that do not require significant structural strength (e.g. palpating tumors, suturing soft tissues, etc.). For instance, multi-tube snake-like MIS systems have been designed and proposed for applications such as drawing blood from the umbilical cord in fetal surgery [5] and procedures benefiting from needle steering [7], [8]. Cable-driven and/or shape memory actuated MIS manipulators have been designed for micro- and neurosurgery [4], micro-grasping in fetal surgery [9], gastro-intestinal interventions [2], [3] and ENT (ear, nose, throat) surgeries [6], [10]–[12]. In our application, however, the DM acts as a guide for flexible tools and must move in a highly viscous environment. Additionally, the DM must overcome the flexing of various tool stems used during this procedure. These requirements must be satisfied while assuming and maintaining small radius "hook-like" shapes to access concavities within and around the acetabular cup. The following sections describe the design, fabrication, and kinematic modeling of a novel DM with the required structural strength, as well as preliminary testing of the manipulator.

II. Manipulator Overview

This section presents the design, fabrication, and actuation decisions taken to create a DM for the less-invasive treatment of osteolytic lesions formed behind the acetabular shell of a THA.

The objective of the DM is to create an actuated tool capable of accessing and cleaning an osteolytic lesion through existing holes in the acetabular component of a THA. Design requirements include: compact size for insertion through existing holes, an open lumen for tool delivery/removal, design and fabrication scalability to fit various sizes/brands of components, high dexterity for tool manipulation and exploration, and relatively large end-effector forces for cleaning procedures involving scraping, brushing, curetting, etc. For the purposes of this preliminary study, we designed our initial prototype to fit the Zimmer Trilogy® acetabular shell (Cat. No. 6200-48-22). This model contains three through holes, each approximately 6.60 mm (0.260 in) in diameter, intended for anchoring screws.

A. Geometry

To ensure a reliable fit through the holes in the acetabular shell, the DM is designed as a modified cylinder with an outer diameter of 5.99 mm (0.236 in). Notches extruded from a common plane allow the DM to bend. Notching in this fashion constrains bending to a single plane parallel to the extrusion plane. By constraining bending to this single plane, there are two potential benefits: (1) simplified manipulator modeling and control (discussed in Section III-B), and (2) an ability to transmit substantial end-effector forces normal to the bend plane without requiring an increase in drive cable tension (discussed in Section IV).

To control bending, two channels are cut axially through the outer wall of the cylinder spaced 180° apart relative to the cylinder axis. Drive cables are threaded through these channels and secured to the end-effector side of the DM. The result is an underactuated hyper-redundant manipulator driven in a marionette-like fashion. That is, applying tension to the left-most cable will cause bending to the left, and applying tension to the right-most cable will cause bending to the right.

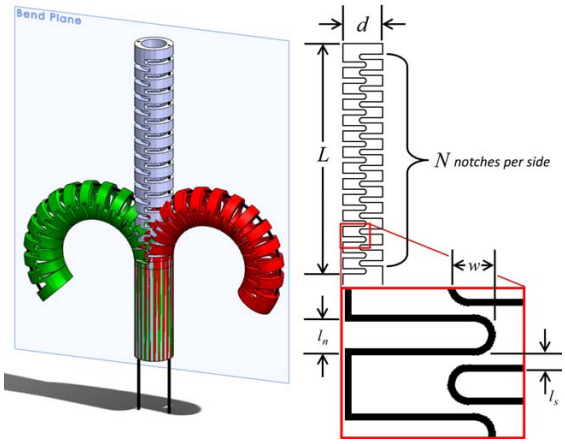

Fig. 2. CAD model of the DM with anticipated bending limits and highlighted bend plane (left) and DM projection onto the bend plane illustrating design variables (right).

The position and geometry of notches in the DM is determined considering a projection of the leg onto the bend plane. Assuming notches are identical, equally spaced, and interleaved, the DM can be characterized using the variables shown on the right side of Fig. 2. With these variables defined:

$$L = (2N + 1)(l_n + l_s) \tag{1}$$

Assuming a simple bending model, we define the maximum bend per notch (α) of the DM using an isosceles triangle with two sides equal to $\frac{d+w}{2}$ and the third equal

to l_n. Defining ϕ as the total DM bend angle, the following equations result:

$$\alpha = 2\sin^{-1}\left(\frac{l_n}{d+w}\right)$$
$$\phi = N\alpha \tag{2}$$

For the purposes of this preliminary design, we fix d as defined above, $l_s = 0.40$ mm (0.0157 in) and $L = 35.00$ mm (1.378 in). Using this, we can define the total bend angle (ϕ) as a function of the total (discrete) number of notches (N) and the notch overlap (w). Since notching is performed using an EDM process, we limit notch thickness (l_n) to at least 0.13 mm (0.005 in). Likewise, because we are considering only manipulator geometries that can explore the full osteolytic lesion, the total bend angle (ϕ) is limited to at least 180° resulting in:

$$\phi = 2N\sin^{-1}\left(\frac{L-(2N+1)l_s}{(2N+1)(d+w)}\right) \tag{3}$$

where $1 \leq N \leq \lfloor (L-(\min(l_n)+l_s))/(2(\min(l_n)+l_s))\rfloor$ and we restrict the notch overlap to $0 \leq w \leq d/2$.

Evaluating 3 within the designated input bounds, and only considering total bend angles between 180° and 360° produces the surface shown in Fig. 3. Intuitively noting that mechanical strain should be proportional to increases in total bend angle and inversely proportional to notch overlap, we initially down select our candidate dimensions to those lying near the 180° lower bound (highlighted with the dashed line).

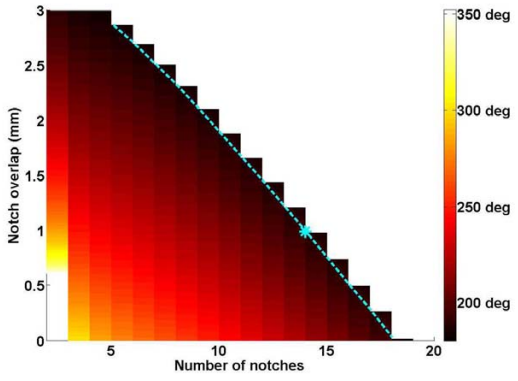

Fig. 3. Plot of bend angle (ϕ) as a function of the total (discrete) number of notches (N) and the notch overlap (w). The leading edge (highlighted with the dashed line) was used as a selection set to consider strain. Selected design parameters are highlighted.

We estimate the strain associated with a full bend for each of the 14 sets of parameters from this leading edge using the finite element package "SolidWorks Simulation." To avoid permanent deformation, we define the design peak strain less than 5% resulting in a safety factor of 1.6 based on the manufacturer recommended value of 8%. Fig. 4 shows that peak strain estimates consistently fall below this 5% strain design constraint. Noting that each candidate is a viable option, we selected the configuration with a moderate notch overlap value near 1.0 mm (0.039 in). The number

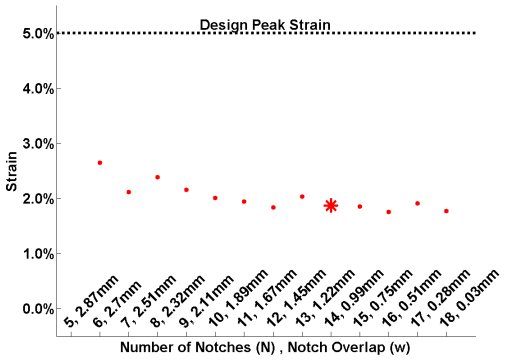

Fig. 4. Maximum strain estimate as a function of the candidate number of notches (N) and notch overlap (w) values. Note that the strain estimate corresponding to $N = 5$ and $w = 2.87$ mm has been excluded due to modeling errors.

of notches, the notch thickness, and the notch overlap are respectively defined: $N = 14$, $l_n = 0.81$ mm (0.032 in), and $w = 0.99$ mm (0.039 in).

B. Fabrication

A key feature in the design of the DM is the tight nesting of the two nitinol tubes to realistically enable the fabrication of the tendon drive holes. In order to ensure proper nesting of tubes, careful manufacturing tolerances were required. The design is based on specification ANSI B4.2-1978(R1999) [13], which describes types of fit dimensions for shafts. The exact specification chosen was "shrink fit, medium drive, shaft basis." The nominal dimensions of the outer tube were 5.99 mm (0.236 in) outer diameter (OD) and 5.00 mm (0.197 in) inner diameter (ID). For the inner tube, 5.00 mm (0.197 in) was chosen for the OD and 3.99 mm (0.157 in) for the ID. These dimensions were chosen to provide an appropriate fit through the screw holes in the acetabular shell (as mentioned previously), and 1 mm (0.039 in)wall thicknesses to provide sufficient room for post-machining in a wire EDM process.

Given these nominal dimensions, the specification suggests 0.007–0.027 mm (0.0003–0.0011 in) of interference, resulting in a final OD for the inner tube of 5.007–5.027mm (0.1971–0.1979 in). With this interference, we planned to heat the outer tube, if necessary, to nest the two tubes during manufacturing. To temporarily expand the outer tube and convert the interference fit to a sliding fit, a change in temperature range of 200–565°C is required. This falls just below the temperature at which nitinol shape-memory "training" occurs.

Fabrication consisted of a four step process: (1) The inner and outer tubes are cut to length on a lathe; (2) The inner tube is mounted (using custom fixtures), and channels are cut on the outside of the inner tube; (3) The outer tube is mounted (using custom fixtures), the EDM wire is threaded through the inner diameter, and channels are cut on the inside of the outer tube; (4) The tubes are nested using two 0.381 mm (0.015 in) gage pins and pressed together using a machine vice; (5) The nested tubes are mounted using a standard

collet and the notches are cut using an EDM process.

C. Actuation

For initial testing, the DM was mounted on a custom Z-θ test rig. To simplify integration and control, stepper motors were used both for controlling manipulator drive cable length and tension, and for controlling the additional Z (linear actuation about the unbent manipulator axis) and θ (spin about the unbent manipulator axis) degrees of freedom (DOF). Based on preliminary hanging weight tests, the maximum required cable tension for an unobstructed full bend in either direction was estimated not to exceed 44 N (10 lbf). As such, Haydon Kerk™ size 14 hybrid linear actuators (Part No. 35H4A-12) were selected to actuate the drive cables. This model offers a resolution of 0.0079 mm/step (0.0003125 in/step) with a recommended load limit of 222 N (50 lbf). Based on the simple bending model described in Section II-A and uniform bending (i.e. equal bending between vertebrae), this step resolution corresponds to a maximum change in total bend angle per step of 0.1524 deg/step.

The Z and θ DOF are each actuated using DMX-UMD-23-3 integrated stepper motors from Arcus Technology Inc. This model actuator offers a maximum torque just above 0.99 Nm (0.73 lbf·ft) near stall (0.84 Nm at 300 RPM) and 200 steps/revolution. Translation in the Z-direction is achieved using a timing belt assembly producing a peak output force of approximately 19.9 N (14.7 lbf) with a translational resolution of 0.00074 mm/step (0.01875 in/step). The θ DOF is actuated through a 1.6:1 gear train. Assuming uniform bending over a total bend angle of 90°, this configuration will result in a peak end-effector force of approximately 44 N (10.0 lbf) in a direction normal to the bend plane of the DM. The custom Z-θ rig is shown in Fig. 5.

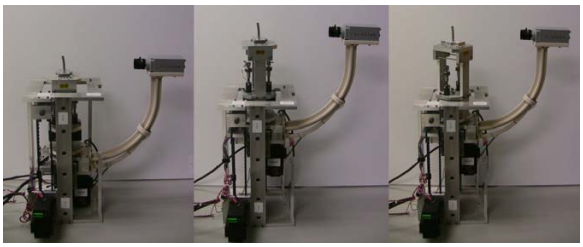

Fig. 5. Images taken of the full Z-θ test rig illustrating the actuated DOF.

D. Electronic Payload and Low-level Control

The Z-θ test rig is outfitted with a series of sensors to help characterize the DM. Each of the DM drive cables connects to its actuator through a 44 N (10 lbf) tension/compression load cell (Honeywell 060-1426-04) amplified using a self-contained bridge amplifier (OMEGA DMD-465). The DM is controlled using the PMX-2ED-SA from Arcus Technology Inc. This 2-axis stepper controller is easily interfaced via USB and contains two 10-bit analog inputs allowing us to measure the amplified load cell signal from each of the DM drive cables. The Z and θ actuators (described in Section II-C) each contain an integrated controller with a USB interface. A CMOS FireWire camera (PixeLINK PL-B774F) with ultra low distortion 16 mm fixed focal length lens (Computar M1620-MPV) is rigidly mounted to the Z portion of the test rig. By rigidly mounting the camera in this fashion, we ensure that the DM remains within the field of view at all times while enabling observation of both θ rotation and bending. Hardware communication is done using Matlab and requires both the Image Acquisition Toolbox and the CMU IEEE 1394 DCAM driver (v6.4.5) to acquire images from the camera.

III. Calibration and Modeling

This section describes the calibration/zeroing procedure and preliminary modeling efforts. Section III-A describes the actuator calibration or zeroing procedure necessary to reliably control the DM and Z-θ stage. Section III-B describes our proposed approach for creating a simple kinematic model of the DM.

A. Manipulator Calibration

The purpose of calibration procedure is to reliably define the zero positions of each of the four actuators relative to the system as a whole. Additionally, we can confirm the ratios of translation/step and rotation/step for the Z and θ actuators, respectively. We address each in ascending difficulty:

1) Z-Calibration: Z-axis calibration relies on two limit switches placed on either end of the permissible range of translation. The Z-axis can be zeroed simply by driving the actuator to each of the two limit switches, and selecting a fixed point within the permissible translation range as the zero.

2) θ-Calibration: θ-axis calibration is performed by bending the DM to an arbitrary position (approximately 90° total bend angle), holding that position, and rotating about the θ axis by approximately 360°, acquiring an image from the camera with every step. Intensity-based segmentation is then performed on each image. The horizontal distances between the left side of the DM's base and the leftmost manipulator pixel, and the right side of the DM's base and the rightmost manipulator pixel are calculated for each image. Assuming negligible lens distortion and a planar projection model, the images corresponding to the largest left and right horizontal pixel distances should occur 180° apart. Using this information, the θ-axis is zeroed with the bending plane set orthogonal to the camera's principal axis. An additional bend and spin procedure with a lesser total bend angle is performed both to confirm the θ-calibration and to estimate the projection of the θ-axis onto the image plane.

3) Drive Cable Length-Calibration: With the θ-axis calibrated, the bending plane is set orthogonal to the camera's principal axis. Each of the two drive cables are countertensioned to 4.4 N (1.0 lbf) and two points are selected on the end-effector (point 29 and 30 in Fig. 6) to estimate the total bend angle relative to the DM axis. The cable on the bend-ward side of the DM is slacked a number of steps proportional to the total bend angle while the opposite cable is actuated to maintain a countertension of

4.4 N (1.0 lbf). The cable on the bend-ward side is then countertensioned to 4.4 N (1.0 lbf), and the total bend angle is again estimated. This procedure is repeated until the total bend angle is approximately zero with each of the drive cables countertensioned to 4.4 N (1.0 lbf). From this point on, we will refer to the drive cable DOF as the *left-axis* and *right-axis* of the system. That is, *tensioning the left-axis results in a leftward bend* in the camera's field of view when the θ-axis is calibrated and zeroed. Similarly, *tensioning the right-axis will result in a rightward bend*.

B. Kinematic Modeling

For the purposes of motion planning, and future design optimization, a simple kinematic model of the system is desirable. The majority of deformation in the DM occurs in a relatively concentrated area between notches. As such, the DM is modeled as a series of pin joints connecting a series of rigid vertebrae. Using images from the camera, we can reliably identify 58 points (P_1, P_2, P_3, ..., P_{58}) on the manipulator (Fig. 6). To compensate for potentially unforeseen effects from countertensioning of cables, we initially designate an independent set of kinematic parameters for the right and left sides of the DM.

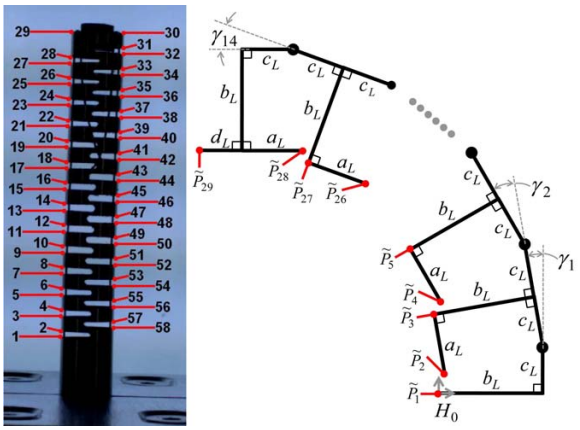

Fig. 6. Selected points used for kinematic modeling: 58 points digitized from each image (left), a representation of the kinematic parameters for the left side of the DM (right).

For the purposes of the kinematic model, we define a separate set of points ($\tilde{P}_1$, $\tilde{P}_2$, $\tilde{P}_3$, ..., $\tilde{P}_{58}$) whose values are derived from a series of kinematic parameters described below. It should be noted that under correct kinematic assumptions and in the absence of errors in point selection, $\|P_i - \tilde{P}_i\| = 0 \; \forall \; i = \{1, 2, 3, \ldots, 58\}$.

Beginning with the left side of the DM, we select a common reference frame $H_0 \in SE(2)$ located at P_1 as follows:

$$H_0 = \begin{pmatrix} R(\gamma_0) & P_1 \\ 0 \quad 0 & 1 \end{pmatrix} \tag{4}$$

where we define $R(\circ) \in SO(2)$ as:

$$R(q_i) = \begin{pmatrix} \cos(q_i) & -sin(q_i) \\ \sin(q_i) & cos(q_i) \end{pmatrix} \tag{5}$$

We define the γ_0 term to align the positive y-direction with the DM axis. Note that by selecting this common reference frame, we set $\tilde{P}_1 = P_1$. From here we define points in pairs of i and $i-1$ for $i = \{3, 5, 7, ...27\}$ as follows:

$$\begin{aligned} \tilde{P}_i &= \tilde{P}_{i-2} + R(q_{i-2})(b_L, c_L)^\intercal + R(q_i)(-b_L, c_L)^\intercal \\ \tilde{P}_{i-1} &= \tilde{P}_{i-2} + R(q_{i-2})(b_L, c_L)^\intercal + R(q_i)(-b_L, x_L)^\intercal \end{aligned} \tag{6}$$

where $q_i = \sum_{j=0}^{\frac{i-1}{2}} \gamma_j$, $x_L = c_L - a_L$, and $R(\circ)$ is defined in 5. A representation of these parameters for $i = \{3, 5\}$ is shown in the bottom right of Fig. 6.

To compensate for the larger offset between $\tilde{P}_{28}$ and $\tilde{P}_{29}$ we assume that the parameter $a_L \propto 2l_s + l_n$. The result is shown in 7:

$$\begin{aligned} \tilde{P}_{29} &= \tilde{P}_{27} + R(q_{27})(b_L, c_L)^\intercal + R(q_{29})(-b_L, c_L + d_L)^\intercal \\ \tilde{P}_{28} &= \tilde{P}_{27} + R(q_{27})(b_L, c_L)^\intercal + R(q_{29})(-b_L, x_L)^\intercal \end{aligned} \tag{7}$$

where $d_L = a_L \frac{3l_s + 2l_n}{2l_s + l_n}$ and x_L is defined above. This is illustrated in the top right of Fig. 6.

Defining the right side of the leg in a similar fashion and using the same common reference frame as described above, we begin by defining $\tilde{P}_{58}$ as follows (assuming $a_R \propto 2l_s + l_n$):

$$\tilde{P}_{58} = \tilde{P}_1 + \frac{a_R}{2l_s + l_n} R(\gamma_0)(d, l_s + l_n)^\intercal \tag{8}$$

From here we again define points in pairs of i and $i+1$ for $i = \{56, 54, 52, ...30\}$ as follows:

$$\begin{aligned} \tilde{P}_i &= \tilde{P}_{i+2} + R(\rho_{i+2})(-b_R, c_R)^\intercal + R(\rho_i)(b_R, c_R)^\intercal \\ \tilde{P}_{i+1} &= \tilde{P}_{i+2} + R(\rho_{i+2})(-b_R, c_R)^\intercal + R(\rho_i)(b_R, x_R)^\intercal \end{aligned} \tag{9}$$

where $\rho_i = \gamma_0 + \sum_{j=\frac{i}{2}}^{28} \gamma_j$, $x_R = c_R - a_R$, and $R(\circ)$ is defined in 5.

The complete model describes the DM motion using a total of 35 terms (a_L, a_R, b_L, b_R, c_L, c_R, γ_0, γ_1, γ_2, ..., γ_{28}).

IV. Preliminary Experimental Results

Two sets of experiments were performed. The first set of experiments, described in Section IV-A, investigates the accuracy of our simplified kinematic model of the system as described in Section III-B. The second set of experiments, described in Section IV-B defines a relationship between end-effector forces and drive cable tension in various configurations of the DM both in and out of the bend plane.

A. Modeling Evaluation

As an initial evaluation of our proposed kinematic model, a series of 120 images of the manipulator in various freely bent configurations were acquired. Within each image, each of the 58 points shown in Fig. 6 was selected. Using this data, we perform a linear least squares fit of the parameters described above on the first 100 images forcing a_L, a_R, b_L, b_R, c_L, and c_R to remain the same for all images, and allowing values of γ_i to be calculated for each image. The resultant error between each of the selected points and point

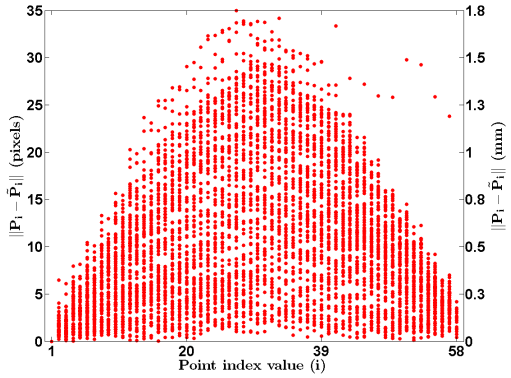

Fig. 7. Error between each of the 58 selected points from the 100 training images and point positions calculated using the imposed kinematic fit. Note that the peak estimated displacement of 35 pixels corresponds to approximately 1.8 mm.

positions calculated using the imposed kinematics is plotted in Fig. 7.

Applying the a_L, a_R, b_L, b_R, c_L, and c_R values calculated using the 100 image training set to a set of 20 additional images, we find that the result remains largely the same (Fig. 8).

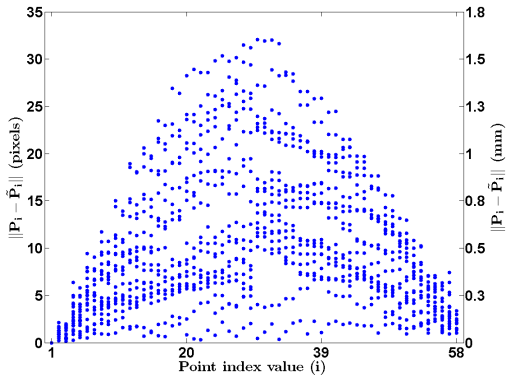

Fig. 8. Error between each of the 58 selected points from the 20 evaluation images and point positions calculated using the imposed kinematic fit. Note that the values of a_L, a_R, b_L, b_R, c_L, and c_R were calculated using the training set only.

B. End-Effector Force Testing

Within the bend plane, a series of seven DM configurations were considered in this initial set of end-effector force tests. Specifically, the following total bend angles were evaluated: $\phi = \{$-135°, -90°, -45°, 0°, 45°, 90°, 135°$\}$. At each of these angles, three loading conditions were applied as shown in Fig. 9 using a Wagner Force One™ FDIX-5 22 N (5 lbf) digital force gauge.

For each bend angle, the test procedure was conducted as follows: (1) Bend the DM to specified total bend angle of interest using procedures similar to those described in Section III-A.3; (2) Change to the correct FDIX-5 tip and align the FDIX-5 to apply an "Eastward" pointing reaction force; (3) Bring FDIX-5 into visible contact with the end-effector while maintaining a 0.00 N reading; (4) Anchor the FDIX-5 in place; (5) Bend the DM on an interval of two steps/data point by tensioning the left-axis; (6) Record tension load cell data, FDIX-5 data, and acquire an image from the camera; (7) Repeat steps 5-6 until a total of 30 data points are acquired; (8) Repeat steps 1-7 for a total of three trials in the specified configuration; (9) Repeat steps 1-7 for the "Westward" pointing reaction force tensioning the right-axis; (10) Repeat steps 1-7 for the "Southward" pointing reaction force tensioning the left-axis, excluding the 0° bend angle; (11) Repeat steps 1-7 for the "Southward" pointing reaction force tensioning the right-axis, excluding the 0° bend angle.

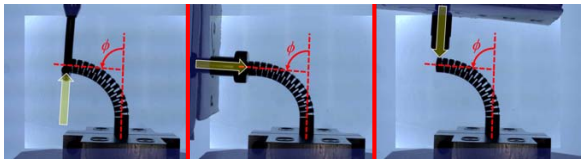

Fig. 9. End-effector force testing within the bend plane: "Eastward" pointing reaction force at total bend angle ϕ (left), "Southward" pointing reaction force at total bend angle ϕ (center), "Westward" pointing reaction force at total bend angle ϕ (right).

For the 0° bend angle with a "Southward" reaction force we quickly noted that tensioning had little to no effect on the reaction force. To compensate, steps 1-7 from above were repeated but the Z-axis was used to increase the reaction force.

The unprocessed results from these tests are shown in Fig. 10, 11, 12, and 13.

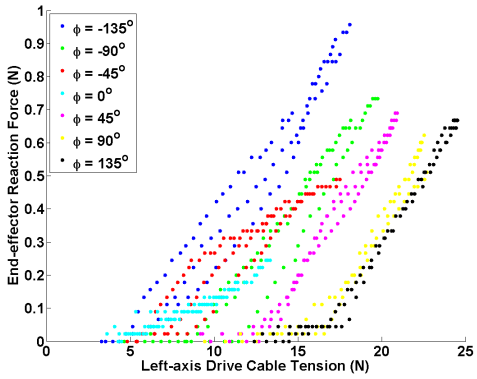

Fig. 10. End-effector force test results given an "Eastward" pointing reaction force within the bend plane.

Outside of the bend plane, only ϕ = -90° was considered, and the θ-axis was rotated 90°, aligning the bend plane with the camera's principal axis and bringing the end-effector closer to the camera. In this configuration, a single loading condition was applied as shown in Fig. 14 using the Wagner Force One™ FDIX-5 22 N (5 lbf) digital force gauge.

The test procedure for testing in this out of plane configuration was conducted as follows: (1) Bend the DM to ϕ = -90° total bend angle using procedures similar to

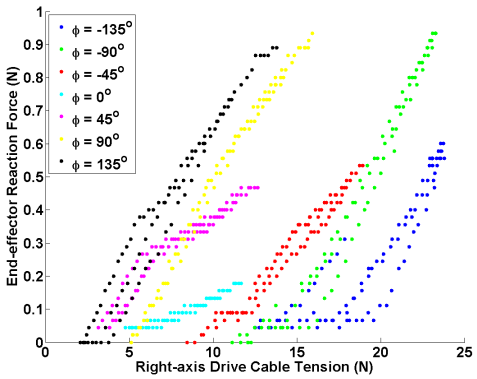

Fig. 11. End-effector force test results given an "Westward" pointing reaction force within the bend plane.

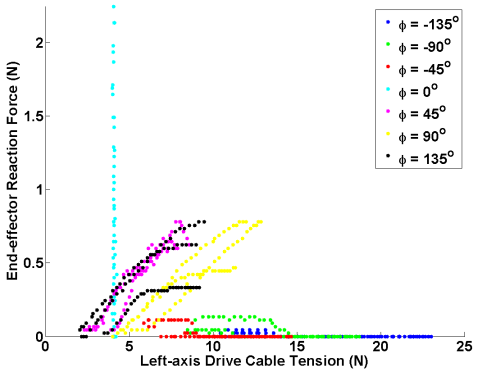

Fig. 12. End-effector force test results given a "Southward" pointing reaction force within the bend plane and tensioning the left-axis drive cable (except in the case of the 0° bend where the Z-axis was used to increase the reaction force).

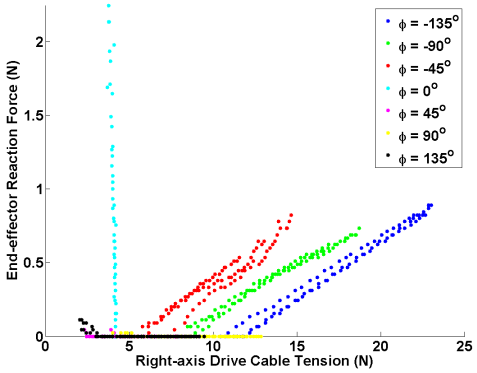

Fig. 13. End-effector force test results given a "Southward" pointing reaction force within the bend plane and tensioning the right-axis drive cable (except in the case of the 0° bend where the Z-axis was used to increase the reaction force).

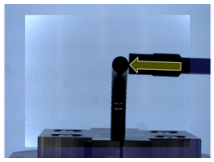

Fig. 14. End-effector force testing outside of the bend plane with a perpendicular reaction force applied and the manipulator fixed at a total bend angle $\phi = 90°$.

those described in Section III-A.3; (2) Rotate the θ-axis 90°, aligning the bend plane with the camera's principal axis and bringing the end-effector closer to the camera; (3) Change to the correct FDIX-5 tip and align the FDIX-5 to apply a load orthogonal to the bend plane; (4) Bring FDIX-5 into visible contact with the end-effector while maintaining a 0.00 N reading; (5) Anchor the FDIX-5 in place; (6) Rotate the θ-axis on an interval of one step/data point towards the point of contact; (7) Record tension load cell data, FDIX-5 data, and acquire an image from the camera; (8) Repeat step 6-7 until a total of 30 data points are acquired; (9) Repeat steps 1-8 for a total of three trials in the specified configuration.

The unprocessed results from these tests are shown in Fig. 15.

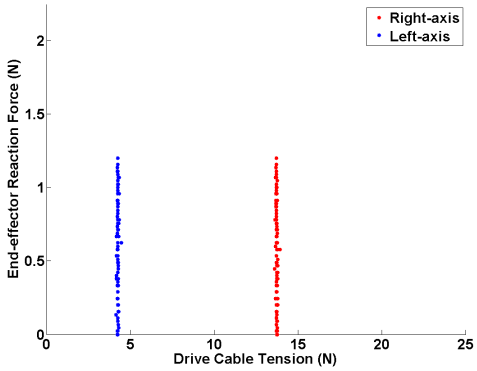

Fig. 15. End-effector force test results given a perpendicular reaction force applied outside of the bend plane with the manipulator fixed at a total bend angle of $\phi = 90°$.

V. Discussion

In this paper we presented the design, fabrication, preliminary control, and modeling of a new dexterous manipulator (DM). The current prototype meets the primary design objectives and functions as expected. The fabrication process has been developed and refined to enable reliable production of prototypes, and offers the possibility of realistic scaling of the design. Bending constrained to a single plain was demonstrated, as well as an ability to apply end-effector reaction forces outside the bend plane without requiring changes in drive cable tension. The DM has yet to show any signs of fatigue or failure despite extensive motion and force testing implying that design peak strain value is not exceeded under standard operation. Preliminary kinematic modeling work has shown that a set of rigid parameters can be used to describe the motion of the DM, and preliminary analysis of end-effector force results implies that predictive dynamic model of the system could be developed.

Based on the results presented in Fig. 7 and 8, the proposed kinematics model the motion of the DM accurately with a peak error of 35 pixels (approximately 1.8 mm) despite the simple preliminary fit used to define parameter values. The seemingly large increase in error near points 29 and 30 is expected because of the model's reference point. That is, the error is additive with each step taken away

from point 1. This result shows no visible increase in error when applying the parameter values derived from the 100 training images to the 20 additional images. From this, one can conclude that a set of rigid parameters derived from a series of training images may be used to reliably describe the motion of the DM. As a future effort, we intend to integrate a constrained minimization algorithm into the fitting of these kinematic parameters.

The purpose of performing end-effector reaction force testing was two-fold: (1) Investigate the possibility of creating a predictive dynamic model of the system relying only on available sensor data; and (2) Investigate the decoupling of cable tension and end-effector forces when end-effector forces are applied out of the bend plane.

From the preliminary in-plane force tests, a proportional relationship is noted between cable tension and end-effector reaction force that is dependent on the DM configuration and loading condition. For both the "Eastward" and "Westward" loading conditions (results shown in Fig. 10 and 11), the end-effector reaction force increases at a near linear rate as the drive cable on the reaction force side is tensioned. Further inspection also suggests that there is a relationship between this rate of increase and the total bend angle of the DM. Specifically, as the magnitude of bend angle ($|\phi|$) increases, the rate tying reaction force to cable tension also increases.

In the "Southward" reaction force testing, additional patterns arise. A coupling between the end-effector forces and tension increases only in the bend-ward cable appears in Fig. 12 and 13. That is, when the DM is bending left ($\phi = \{45°, 90°, 135°\}$), only increases in the left-axis tension result in an increase in end-effector force. Likewise, when the DM is bending right ($\phi = \{\text{-}45°, \text{-}90°, \text{-}135°\}$), only increases in the right-axis tension result in an increase in end-effector force.

For the end-effector forces applied outside the bend plane, the results exactly match expected design functionality of the manipulator. That is, both the left-axis and right-axis cable tensions remain constant as the end-effector reaction force increases (shown in Fig. 15). A similar behavior is noted in both the left-axis and right-axis drive cables in all three trials of the "Southward" force testing when $\phi = 0°$ (Fig. 12 and 13) indicating that, within the prescribed loading range, the manipulator withstands axial loading without noticeably deforming.

From this force testing, we can conclude that creating a predictive dynamic model of the manipulator relying on cable tension and length measurements is possible, however there is a fair amount of variability between trials under identical conditions. Additionally, we have shown that within the constrained loads of this testing, decoupling of cable tension and end-effector forces occurs both when end-effector forces are applied out of the bend plane, and when a "Southward" end-effector force is applied when the DM is at a total bend angle of $\phi = 0°$. This information implies that additional sensors will be required on both the Z and θ axes for accurate modeling of the system.

While the results discussed in this paper describe a functional prototype that meets the specified design goals, there are still a series of limitations that are yet to be addressed. Preliminary path planning work utilizing a simple kinematic model to describe a comparable manipulator's motion has demonstrated 85–95% coverage rates of surgically relevant osteolytic cavities. While this number suggests better performance than those described in [1], it indicates that further improvements can and should be made to the manipulator. Of these, further optimization of the manipulator geometry as well as the possibility of multi-mode and 3D bending through an increase in the number of drive cables and out of plane notch placement will be considered in future works.

VI. ACKNOWLEDGMENTS

The authors thank Mr. David Athman for his expertise and insight as applied to the machining and assembly of the DM, Mr. Jason Glasser for his design and fabrication efforts on the Z-θ rig, Mr. Chester Chambers for his manual processing of countless images, and Mr. Ryan Murphy for his review of this work.

REFERENCES

[1] C. A. Engh, Jr., H. Egawa, S. E. Beykirch, R. H. Hopper Jr., and C. A. Engh, "The quality of osteolysis grafting with cementless acetabular component retention," *Clinical orthopaedics and related research*, vol. 465, pp. 150–154, Dec. 2007.

[2] P. Dario, M. Carrozza, M. Marcacci, S. D'Attanasio, B. Magnami, O. Tonet, and G. Megali, "A novel mechatronic tool for computer-assisted arthroscopy," *Information Technology in Biomedicine, IEEE Transactions on*, vol. 4, no. 1, pp. 15–29, Mar. 2000.

[3] D. Reynaerts, J. Peirs, and H. Van Brussel, "Shape memory micro-actuation for a gastro-intestinal intervention system," *Sensors and Actuators A: Physical*, vol. 77, no. 2, pp. 157–166, Oct. 1999.

[4] K. Ikuta, K. Yamamoto, and K. Sasaki, "Development of remote microsurgery robot and new surgical procedure for deep and narrow space," in *Robotics and Automation, 2003. Proceedings. ICRA '03. IEEE International Conference on*, vol. 1, Sep. 2003, pp. 1103–1108.

[5] J. Furusho, T. Katsuragi, T. Kikuchi, H. Suzuki, H. Tanaka, Y. Chiba, and H. Horio, "Curved multi-tube systems for fetal blood sampling and treatments of organs like brain and breast," *Journal of Computer Assisted Radiology and Surgery*, vol. 1, pp. 223–226, 2006.

[6] A. T. Hillel, A. Kapoor, N. Simaan, R. H. Taylor, and F. P., "Applications of robotics for laryngeal surgery," *Otolaryngologic Clinics of North America*, vol. 41, no. 4, pp. 781–791, Aug. 2008.

[7] R. Webster, J. Romano, and N. Cowan, "Mechanics of precurved-tube continuum robots," *Robotics, IEEE Transactions on*, vol. 25, no. 1, pp. 67–78, Feb. 2009.

[8] P. Sears and P. Dupont, "Inverse kinematics of concentric tube steerable needles," in *Robotics and Automation, 2007 IEEE International Conference on*, Apr. 2007, pp. 1887–1892.

[9] K. Harada, K. Tsubouchi, M. Fujie, and T. Chiba, "Micro manipulators for intrauterine fetal surgery in an open mri," in *Robotics and Automation, 2005. ICRA 2005. Proceedings of the 2005 IEEE International Conference on*, Apr. 2005, pp. 502–507.

[10] N. Simaan, R. Taylor, and P. Flint, "High dexterity snake-like robotic slaves for minimally invasive telesurgery of the upper airway," in *Medical Image Computing and Computer-Assisted Intervention. MICCAI 2004*, vol. 3217, 2004, pp. 17–24.

[11] N. Simaan, K. Xu, W. Wei, A. Kapoor, P. Kazanzides, R. Taylor, and P. Flint, "Design and integration of a telerobotic system for minimally invasive surgery of the throat," *The International Journal of Robotics Research*, vol. 28, no. 9, pp. 1134–1153, Sep. 2009.

[12] J. Peirs, D. Reynaerts, H. Van Brussel, G. De Gersem, and H.-W. Tang, "Design of an advanced tool guiding system for robotic surgery," in *Robotics and Automation, 2003. Proceedings. ICRA '03. IEEE International Conference on*, vol. 2, Sep. 2003, pp. 2651–2656.

[13] E. Oberg, F. D. Jones, H. L. Horton, and H. H. Ryffel, *Machinery's Handbook*, 27th ed. New York: Industrial Press, Inc., 2004, pp. 665–677.